Morphological transformation of arched ribbon driven by torsion

Yuanfan Dai[a,1], Bohua Sun[a,*], Yi Zhang[a] and Xiang Li.[a]

[a]*School of Civil Engineering & Institute of Mechanics and Technology, Xi'an University of Architecture and Technology, Xi'an 710055, China*

ARTICLE INFO

ABSTRACT

The morphological transformation of an arched ribbon driven by torsion is a scientific problem that is connected with daily life and requires thorough analysis. An arched ribbon can achieve an instantaneous high speed through energy transformation and then return to the original shape of the structure. In this paper, based on the characteristics of the ribbon structure, the dynamic mathematical model of the arched ribbon driven by torsion is established from the Kirchhoff rod equation. The variations of the Euler angle of each point on the center line of the ribbon with the arc coordinate s and the rotation angle of the supports ϕ was examined. The relationship between the internal force distribution of each point in the direction of $\hat{d}_a$ and the material, cross-sectional properties, and rotation angle of the supports was obtained. We used ABAQUS, a nonlinear finite element analysis tool, to simulate the morphological transformations of the ribbons, verified our theory with simulation results, and reproduced the experimental results of Sano. Furthermore, we redefined the concept of the "critical flipping point" of Sano. In this paper, the dimensional analysis method was used to fit the simulation data. The following relationship between the critical width w^*, thickness h, and the radius R of the ribbon with different cross sections was obtained: $w^* = A \cdot R(h/R)^{0.6}$, where A is 3.19 for rectangular cross sections and 3.06 for elliptical cross sections. By analyzing the simulation data, we determined the variation behavior of the out-of-plane deflection of the center point of the ribbon with the radius R, width w, and thickness h. Our research has guiding significance for understanding and designing arched ribbons driven by torsion, and the results can be applied to problems of different scales.

Contents

*Corresponding author.

✉ sunbohua@xauat.edu.cn (.B. Sun); Mobile:+86 15001102877 (.B. Sun)

🌐 imt.xauat.edu.cn (.B. Sun)

1. Introduction

A piece of paper is held at both ends so that it forms an arc. When both ends of the strip are rotated inward at the same time, the strip first deflects, then recoils, and finally flips quickly back to its previous shape, as shown in Fig. 1.

Through the rotation applied by the hands to both ends of the paper strip, the shape of the paper strip can be rapidly changed. This phenomenon is actually caused by deformation energy being converted into kinetic energy. First, the paper strip slowly stores the torsional energy applied by the hands as rotational deformation energy. It then releases the accumulated rotational deformation energy quickly at a certain critical point and converts it into kinetic energy, and finally, it completes the "flip."

To survive and develop, some plants and fungi (Skotheim and Mahadevan, 2005; Forterre, 2013) take advantage of this rapid transformation mechanism. They store deformation energy through some of their own components and then release this energy to increase the speed instantly, e.g., the predation behavior of flycatchers (Fortorre, Skotheim, Dumais and Mahadevan, 2005). People have also proposed designs with specific functions through
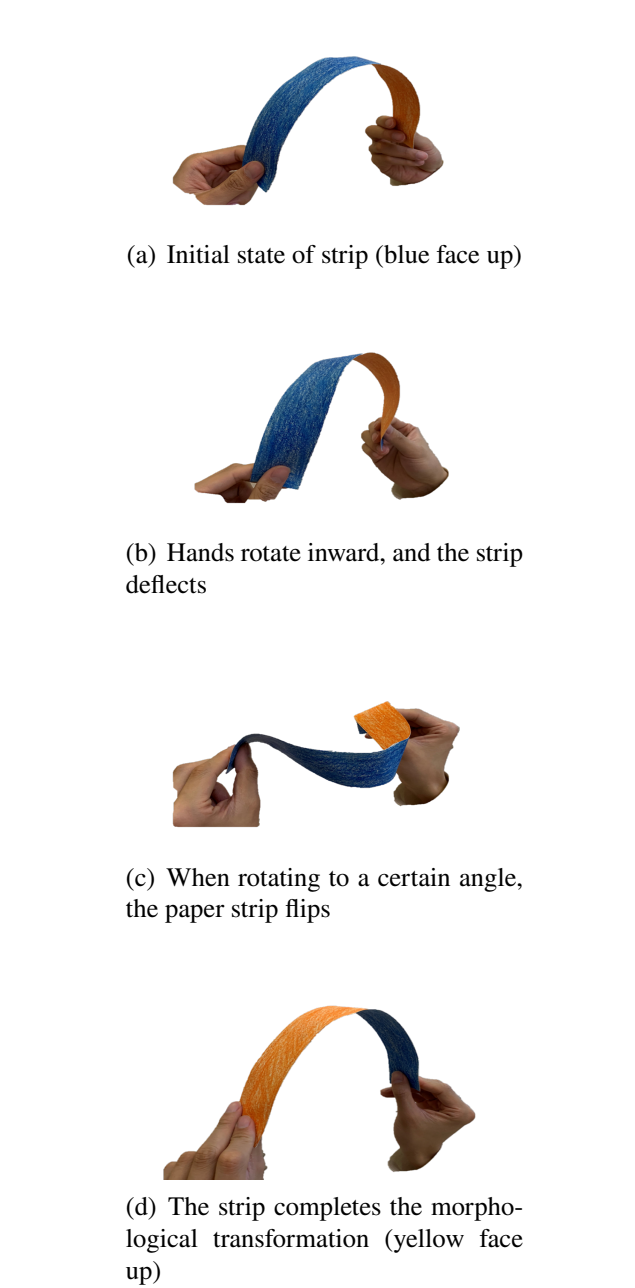

(a) Initial state of strip (blue face up)

(b) Hands rotate inward, and the strip deflects

(c) When rotating to a certain angle, the paper strip flips

(d) The strip completes the morphological transformation (yellow face up)

Figure 1: Process of morphological transformation of strip.

this mechanism. Deepak, Rahn, Kier and Walker (2008) designed a novel soft robot with a rapid change of this form, which had more freedom and faster response speeds because of its flexibility. Yuk, Lin, Ma, Takaffoli, Fang and Zhao (2017) used this mechanism to design a new hydrogel driver, which could produce greater speeds and forces than the traditional driver under water and had better camouflage. Inspired by the Venus flytrap, Holmes and Crosby (2007) designed a simple, robust, and

responsive surface that allowed rapid changes in morphology, with adjustable transition times, sensitivity, and amplitude changes.

Sano and Wada (2019) studied the structures of ribbons driven by torsion, established a theoretical model to predict the change of the the out-of-plane deflection of the center point of the ribbon with the rotation angle of the supports, and proposed the relationship between the critical width of the ribbon and its thickness and radius. Sano's research is of great significance for guiding the design of ribbon structures. However, Sano selected less data for the prediction of the critical width formula and did not carry out an in-depth study on the rate of change of displacement relative to rotation angle $dy/d\phi$ during ribbon flipping. The rapid morphological transformation process of a ribbon is always accompanied by nonlinear and large deformations. To obtain the mechanical information of the whole deformation process more accurately, we used the nonlinear finite element analysis tool ABAQUS to simulate the process and revealed the general process of the ribbon morphological transformation driven by torsion.

Starting from the theory of elastic plates, Audoly and Neukirch (2021) established a non-linear one-dimensional model for elastic ribbons. This model adopted the form of a rod model, had a special non-linear constitutive law, and took into account the stretching and bending of the ribbon midsurface. It bridged the gap between Kirchhoff model and Sadowsky model. It unified these two models into a single framework, allowing them to be recovered as limiting situations.

First, a mathematical model of the dynamics of an arched ribbon driven by torsion is established, and the variations of the Euler angle of each point on the center line of the ribbon with the arc coordinate s and rotation angle of the supports ϕ are deduced. Next, the theoretical model and the experimental results of Sano are verified using the finite element software ABAQUS to ensure the reliability of the simulation. We then obtained the relationship between the critical width of "flipping" w^*, the thickness h, and the curvature radius R of the ribbon with different cross sections by means of dimensional analysis. The general variation rate of the center point displacement relative to the rotation angle $dy/d\phi$ with the radius R, width w, and thickness h is then studied. Finally, conclusions are provided.

2. Dynamics of arched ribbon driven by torsion

Considering the geometric characteristics of the ribbon, this paper regards the ribbon as a curved arch structure, and the schematic diagram of the arch structure is shown in Fig. 2.
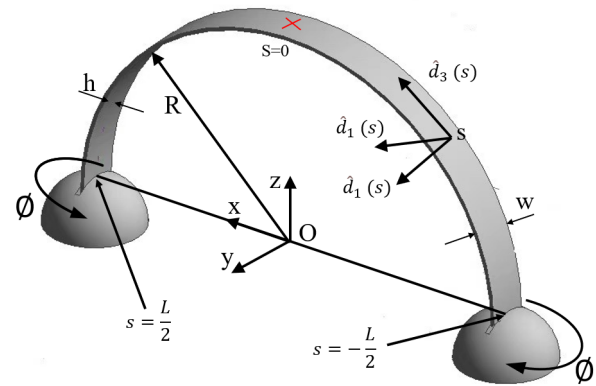

Figure 2: Schematic diagram of the model of an arched ribbon driven by torsion and definition of the coordinate system.

2.1. Dynamic model of arched ribbon driven by torsion

This analysis begins with the Kirchhoff rod equation with an inertia term (Kirchhoff, 1859):

$$\frac{\partial F}{\partial s} + f_v - \rho \, \mathrm{Sg} \, \hat{z} = \rho S \frac{\partial^2 r(s,t)}{\partial t^2}, \qquad (1)$$

$$\frac{\partial M}{\partial s} + \hat{d}_3 \times F + m_v \hat{d}_3 = \frac{\partial L(s,t)}{\partial t}, \qquad (2)$$

where ρ is the density, S is the cross-sectional area, and g is the gravitational acceleration. In Eq. 2, $L(s,t)$ represents the angular momentum density per unit length, which is given by $L = I_a \omega_a d_a$, where $\omega(s,t) = \omega_a \hat{d}_a$ is the angular velocity vector at s, and I_1 and I_2 are the principal moments of inertia of the cross section. For narrow ribbons, $I_1 = \rho s w^2/12$, $I_2 = \rho s h^2/12$, and $I_3 = I_1 + I_2$. The force density f_v and axial torque density $m_v \hat{d}_3$

represent the resistance and moment, respectively, acting on the center line of each length of the ribbon from the background medium. We assumed $\boldsymbol{f}_v = -\gamma_t \boldsymbol{v}$ and $m_v = -\gamma_r \omega_3$ with $\omega_3 = \boldsymbol{\omega} \cdot \hat{\boldsymbol{d}}_3$, where γ_t and γ_r are air resistance friction coefficients.

The new spatial framework $\hat{d}_a (a = 1, 2, 3)$ must follow the following spatial and temporal kinematics equation (Powers. and Thomas, 2010):

$$\frac{\partial \hat{d}_a}{\partial s} = \Omega \times \hat{d}_a, \quad \frac{\partial \hat{d}_a}{\partial t} = \omega \times \hat{d}_a. \tag{3}$$

Along the Ω_a is d_a in the direction of rotation speed. Combining the constitutive relations $M_1 = A_1 \Omega_1$, $M_2 = A_2 \Omega_2$, and $M_3 = C\Omega_3$ (Sano and Wada,2019), where A_1 and A_2 are bending moduli and C is the torsion modulus ($A_1 = Ehw^3/12$; $A_2 = Eh^3w/12$; $C = Eh^3w/(1 + v)$) (Holmes and Crosby,2007), and the expression $\boldsymbol{M}' = M_a' \boldsymbol{d}_a + M_a \boldsymbol{d}_a'$, the following expression for $\boldsymbol{M}'$ can be obtained:

$$\begin{aligned} \boldsymbol{M}'(s) = &[M_1' + (M_3\Omega_2 - M_2\Omega_3)]\hat{d}_1 \\ &+[M_2' + (M_1\Omega_3 - M_3\Omega_1)]\hat{d}_2 \\ &+[M_3' + (M_2\Omega_1 - M_1\Omega_2)]\hat{d}_3 \end{aligned} \tag{4}$$

Substituting Eq. 3 and Eq. 4 into Eq. 2, we obtain the following:

$$\begin{aligned} (A_2 - A_1)&\Omega_1\Omega_2 + C\frac{\partial \Omega_3}{\partial s} - \gamma_r \omega_3 \\ &= \left(I_2 - I_1\right) w_1 w_2 + I_3 \frac{\partial w_3}{\partial t}. \end{aligned} \tag{5}$$

If the air resistance is ignored, Eq. 5 will have high symmetry, which is of great significance for studying the dynamics of ribbons. In this paper, Eq. 5 is rewritten by using instantaneous relation $\partial \phi / \partial t = w_3$:

$$\begin{aligned} (A_2 - A_1)&\Omega_1\Omega_2 + C\frac{\partial \Omega_3}{\partial s} - \gamma_r \omega_3 \\ &= \left(I_2 - I_1\right) w_1 w_2 + I_3 \frac{\partial^2 \phi}{\partial t}. \end{aligned} \tag{6}$$

Meanwhile, by introducing the internal force per unit length $f = \partial F / \partial s$, Eq. 3 can be rewritten as follows:

$$\boldsymbol{f} = \rho S \frac{\partial^2 \boldsymbol{r}}{\partial t^2} + \gamma_t \frac{\partial \boldsymbol{r}}{\partial t} + \rho \boldsymbol{S} g \hat{z}. \tag{7}$$

Eq. 6 and Eq. 7 constitute our dynamics model of the ribbon structure. In the arched ribbon model in this paper, we do not consider any external forces (including gravity and air resistance). Therefore, Eq. 1 and Eq. 2 can be rewritten as follows:

$$\boldsymbol{F}'(s) = 0. \tag{8}$$

$$\boldsymbol{M}'(s) + \hat{\boldsymbol{d}}_3 \times \boldsymbol{F} = 0. \tag{9}$$

It can be deduced that

$$\begin{aligned} F_1 &= -A_2\frac{\partial \Omega_2}{\partial s} - \left(A_1 - A_3\right)\Omega_1\Omega_3, \\ F_2 &= A_1\frac{\partial \Omega_1}{ds} + \left(A_3 - A_2\right)\Omega_2\Omega_3, \\ F_3 &= A_3\frac{\partial \Omega_3}{ds} + \left(A_2 - A_1\right)\Omega_1\Omega_2 = 0. \end{aligned} \tag{10}$$

2.2. Variations of Euler angles with fixed end rotation angle ϕ and arc coordinate s during ribbon movement

We can also use the Euler angles φ, θ, and ψ to represent Ω_a, where φ, θ, and ψ represent the azimuthal, polar, and twist angles, respectively. It can be deduced that $\Omega_1 = \frac{d\varphi}{ds}\cos\theta\sin\psi - \frac{d\theta}{ds}\cos\psi$, $\Omega_2 = \frac{d\varphi}{ds}\cos\theta\cos\psi + \frac{d\theta}{ds}\sin\psi$, and $\Omega_3 = \frac{d\varphi}{ds}\sin\theta + \frac{d\psi}{ds}$.

Eq. 10 is highly nonlinear, which is not conducive to obtaining a solution. Sano and Wada (2019) simplified the problem into a linear problem by retaining the second-order term in the elastic deformation energy of the ribbon $E_{\text{ribbon}} = \int ds(A_1\Omega_1^2 + A_2\Omega_2^2 + C\Omega_3^2)/2$ and taking $h/w \to 0$, yielding the Euler–Lagrange equations in terms of $\psi(s)$ and $\theta(s)$:

$$\begin{cases} \frac{d\theta}{ds} = \frac{1}{R}\psi(s), \\ \frac{d^4\psi}{ds^4} + \frac{3-v}{2R^2}\frac{d^2\psi}{ds^2} + \frac{1}{R^4}\psi(s) = 0. \end{cases} \tag{11}$$

The boundary conditions are $\psi'(0) = \psi'''(0) = 0$, $\psi(\frac{\pi R}{2}) = \psi(-\frac{\pi R}{2}) = -\phi$, $\psi(0) = \frac{2\phi}{\pi}$, $\theta(0) = 0$. In particular, when the Poisson's ratio is $v = -1$, the solution of the equation exhibits the best convergence. We express the solution in terms of hyperbolic functions as follows:

$$\psi(s) = 2\frac{\phi}{\pi}\left[\cosh\left(\frac{s}{R}\right) - 1.13\frac{s}{R}\sinh\left(\frac{s}{R}\right)\right],$$

$$\theta(s) = 2\frac{\phi}{\pi}\left[2.13\sinh\left(\frac{s}{R}\right) - 1.13\frac{s}{R}\cosh\left(\frac{s}{R}\right)\right],$$

$$(12)$$

where $\sinh x = (e^x - e^{-x})/2$, and $\cosh x = (e^x + e^{-x})/2$.

With Eq. 12, we can predict the Euler angle change of each point on the center line of the ribbon and further deduce that the internal force distribution of each point in the direction of $\hat{d}_a$ is related to the material of the ribbon, the cross section attributes, and the rotation angle of the supports. Because our theory is based on Kirchhoff model (Dill, 1992) instead of Sadowsky model (Chopin, Démery and Davidovitch, 1929), it is more accurate when w/h is less than 20. To verify the correctness of our conclusion, we will compare the theory with the finite element method in the next section.

3. Finite element simulation of arched ribbon structure under torsional actuation

Our theoretical model is actually a simplified model within the framework of linear elasticity. This model cannot fully capture the highly nonlinear behavior of the morphological transformation of the arched ribbon driven by torsion, and thus, we need to use a more complex model to study it. Therefore, we selected the nonlinear finite element analysis tool ABAQUS to analyze this problem. In this paper, the numerical simulation method is compared with our theoretical structure and Sano's experimental results (Sano and Wada,2019) to verify the feasibility of the finite element model. In the numerical simulation process, shell elements were used for the ribbon, and the element type was S4R. The ribbon material was the same PET (polyethylene terephthalate) material as that used in Sano's experiment, which was convenient for comparison and verification. The influences of gravity and air resistance were ignored in the simulation. Fig. 3 shows the schematic diagram of the specific finite element model.

3.1. Definition of "flip point"

By applying a small angle ϕ to the supports, the ribbon will deflect from the original plane of the curve, unfurling left-handed and right-handed helices symmetrically on both sides. With the increase in ϕ, the ribbons with different widths w
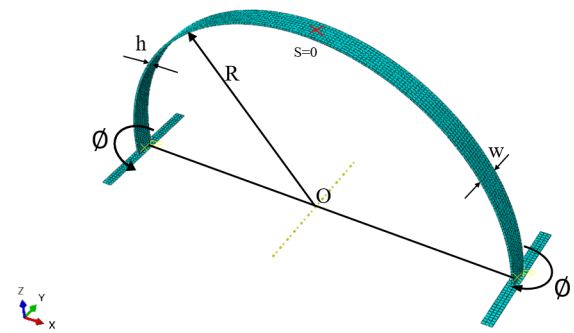

Figure 3: Finite element model of arched ribbon.

exhibited different motion modes. The narrow ribbon ($w < w^*$) recoiled and eventually flipped back to its original configuration, but the inward-facing surface turned outward. The wider ribbon ($w > w^*$), where w^* represents the critical width) did not flip over.Sano and Wada (2019) explained this as follows. In a narrow ribbon, the helices on the two sides have opposite shapes. As the angle ϕ increases, the pair of helices collide and cancel at the center, triggering a flip. A sufficiently wide ribbon forms a local helix near the supports at both ends. As ϕ increases, the curvature of the middle part of the ribbon gradually decreases. This pair of helices gradually tends to be stable, thus forming a crease or kink (Yu and Hanna,2019). Sano and Wada (2019) called this movement mode "folding" and the former "flipping." We will follow this naming convention for the sake of consistency. Sano and Wada (2019) defined the "flipping point" as the moment when the torque applied to the fixed end was zero, while in this paper, it is defined as the moment when the maximum bending moment of the support is perpendicular to the cross-sectional direction, which is more accurate and convenient to locate in the study of ribbons.

3.2. Comparison between simulation results and theory

We compared the results of the finite element simulation with the theoretical results of the first part of this paper (the ribbon size was selected as (h, w, R) = (1, 10,100 mm), as shown in Fig. 4 and Fig. 5.

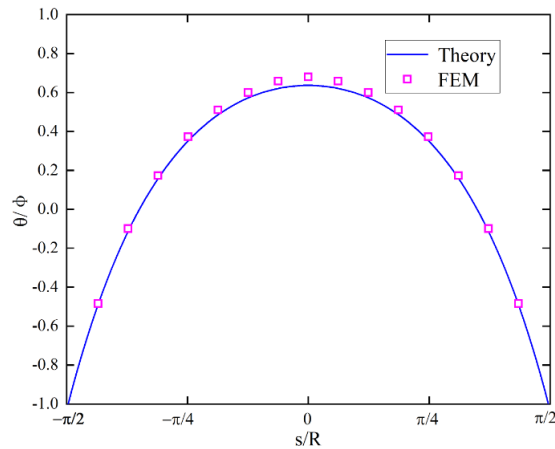The deviations between the finite element and theoretical results were very small, which not only

Figure 4: Relationship between the ratio of the twist angle to the fixed end rotation angle ψ/ϕ and the ratio of the arc coordinate and radius s/R.
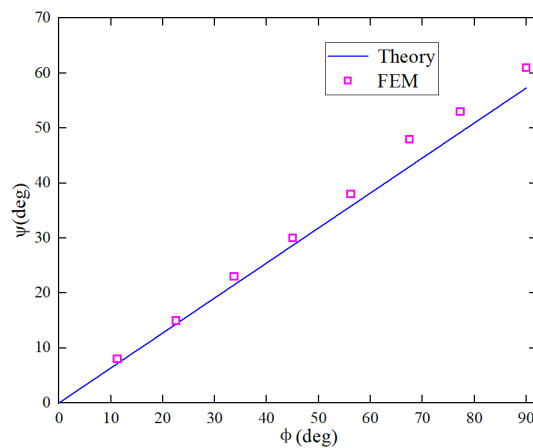

Figure 5: Relationship between the twist angle ψ and the rotation angle of the supports ϕ at the center point $s = 0$ of ribbon.

showed the accuracy of the theoretical results but also verified the reliability of the finite element study on this problem. However, the numerical results also showed that in the first part of the theoretical analysis, the analytical solution obtained by simplifying the equation as linear was not perfect. To obtain more accurate results, it is necessary to consider the role of nonlinear factors.

3.3. Comparison between simulation results and experiments

To record the shape change of the ribbon, we take a specific point ($s = 0$) on the center line of the ribbon as the recording point to draw its out-of-plane deflection y_0. For a narrow ribbon

($w < w^*$), y_0 decreased linearly with ϕ at first and then increased sharply before and after flipping, as shown in Fig. 6(a). For a wide ribbon ($w > w^*$), y_0 also decreased first and then increased, but the value was negative over the whole process (Fig. 6(b)). We successfully simulated the inversion morphological transformation, and the data were in good agreement with the experimental data of (Sano and Wada,2019) (triangles in Fig. 6). After "flipping," the displacement of the numerical simulation was larger than the experimental value, because it was affected by various external factors in the experiment, such as air resistance, gravity, asymmetry of the bearing rotation at both ends, and mechanical wear error. In the finite element simulations, these factors were absent, so the obtained displacement was larger.

In further research, Sano and Wada (2019) deduced that the shape of the center line could be expressed by the following equation:

$$y_0 \simeq -\left(1 - \frac{2}{\pi}\right)\phi R. \tag{13}$$

This prediction (solid lines in Fig. 6) was also highly consistent with our numerical results, which again verified the reliability of the finite element simulation. However, Sano did not perform an in-depth study on the sudden change of the out-of-plane deflection y_0 before and after the "flipping." We will discuss this in Section 4.

4. Discussion on critical width w^* of ribbons with different cross sections

After verifying the feasibility and reliability of the numerical simulation in the previous section, further research on ribbon was performed using this method.

4.1. Discussion of ratio of in-plane stretch elasticity to Kirchhoff strain energy $E_{\text{str}}/E_{\text{Kirch}}$

The mechanical equilibrium of a ribbon is determined by the energetic balance between bending and twisting (Sadowsky, 2016). The torsional deformation energy of ribbon consists of two parts, $E_{\text{twist}} = E_{\text{Kirch}} + E_{\text{str}}$, where the former is the linear Kirchhoff strain energy over the thickness of the ribbon and the latter is from the in-plane
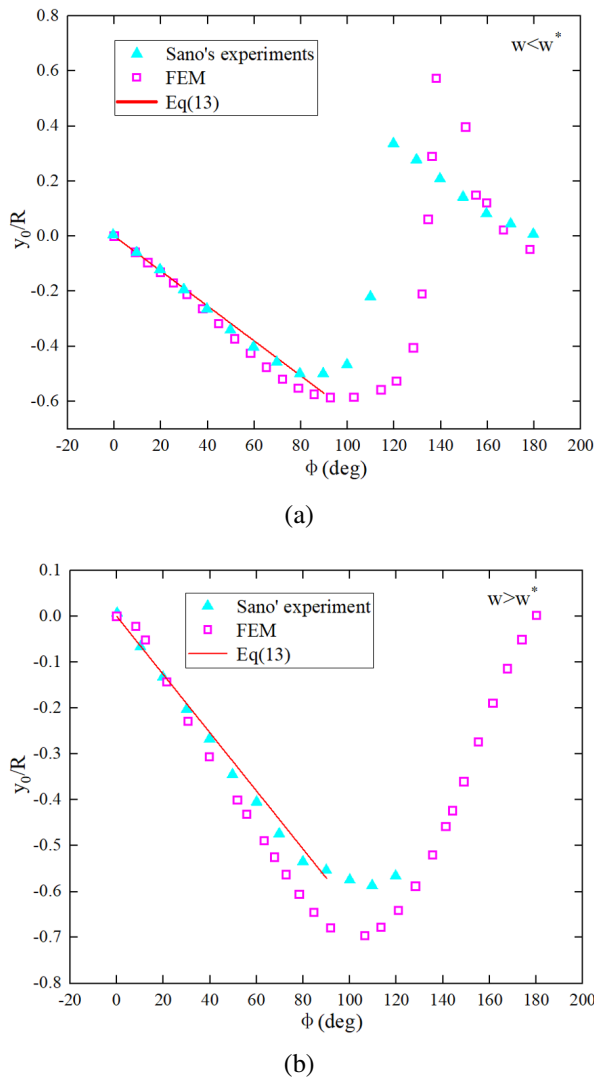
(a)

(b)

Figure 6: Comparison of the finite element simulation, theoretical, and experimental results. The independent variable is ϕ, and the dependent variable is y_0/R. The size of the ribbon is the same as that in the experiment of Sano for (a) a narrow ribbon with $(h, w, R) = (0.2, 8, 108 \text{ mm})$ and for (b) a wide ribbon with $(h, w, R) = (0.2, 15, 108 \text{ mm})$.

The squares and triangles represent the finite element simulation data and the experimental data, respectively, and the solid red line is the prediction using Sano's formula.

stretching elasticity (Pomeau. and Yves., 2010; Ghafouti and Bruinsma, 2005; Grossman, Sharon and Diamant, 2016; Armon, Aharoni, Moshe and Sharon, 2014). In an equilibrium state, $E_{\text{bend}} \simeq E_{\text{twist}}$, where E_{bend} is the bending energy of the ribbon. We simulated Kirchhoff rods ($E_{\text{str}} = 0$) with

w/h close to 1 and found that they all "flipped." Therefore, if $E_{\text{kirch}} \gg E_{\text{str}}$, then $E_{\text{kirch}} \simeq E_{\text{bend}}$, and the ribbon will flip at ϕ^*. This is a narrow ribbon situation, where $w < w^*$. In contrast, for sufficiently wide ribbons, the in-plane stretch elasticity E_{str} contributed significantly to E_{twist}, and then $E_{\text{str}} \simeq E_{\text{Kirch}}$. The movement of the ribbon made it more like an expandable surface, which would be folded. Therefore, determining the relationship between E_{Kirch} and E_{str} enables us to determine the boundary between the flipping and folding phenomena. In our ribbon structure, the typical twist is scaled as $\tau \simeq \phi/R$, and the Kirchhoff strain energy per unit length is given by $E_{\text{Kirch}} = C\tau^2/2 \simeq Eh^3w\phi^2/\left[12(1+\nu)R^2\right]$. For local helicoids, the Gaussian curvature is τ^2, and the in-plane strain is $\epsilon \simeq w^2\tau^2$. The accurate analysis of the helicoid gives the stretching energy per unit length $E_{\text{str}} = Ehw^5\phi^4/\left(1440R^4\right)$ (Sadowsky, 2016; Green, 1936). Sano speculated that the ribbon may turn over when $E_{\text{bend}} \simeq E_{\text{Kirch}} > E_{\text{str}}$ and $\phi \simeq \phi^*$, which is expressed as follows:

$$w < w^* \simeq \left(\frac{120}{(1+\nu)\phi^{*2}}\right)^{1/4} \sqrt{Rh}. \quad (14)$$

When $\phi^* = 115°$, $\nu = 0.3$, and $w^* \simeq 2.2\sqrt{Rh}$. ν was set to 0.3 because Sano proved that the critical width was less sensitive to Poisson's ratio. $\phi^* = 115°$ because the turning angles of the different ribbons were roughly 115°. To verify the correctness of this conclusion, we used Python to carry out finite element simulations on ribbons with different radii. By changing the length w and width h of the ribbon cross section, we obtained multiple sets of experimental results, which made the conclusion more accurate and highly reliable. We improved the accuracy of the critical width to 0.05 mm. Fig. 7 shows a comparison between our results and Eq. 14.

In the two figures, two dimensionless quantities, h/R and w/R, were taken as the independent and dependent variables, respectively. For the same values of the independent variables, the dependent variables of the arched ribbons with radii of 100 and 70 mm were almost equal, which showed that the radius of ribbons did not have an additional influence on the equation and the framework
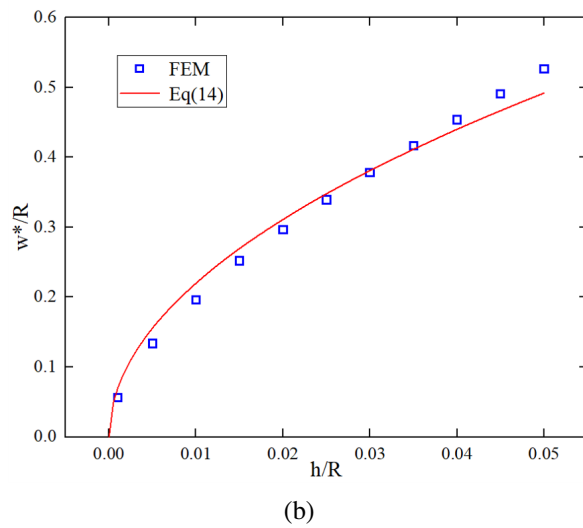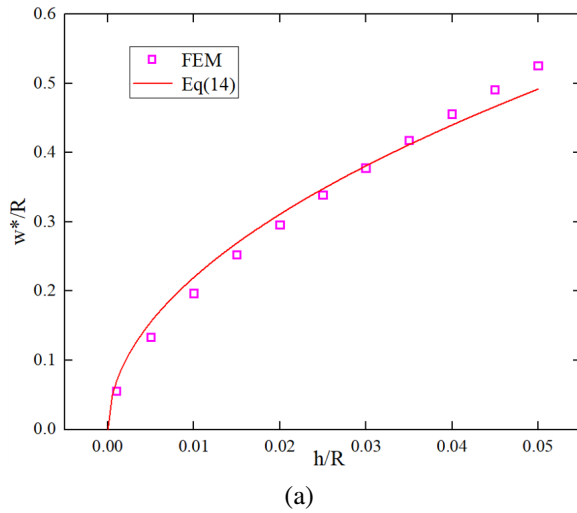
(a)

(b)

Figure 7: Comparison of simulation data and Eq. 14 for ribbon radii of (a) 100 mm and (b) 70 mm.

(a) h/R=0.1

(b) h/R=0.3

(c) h/R=0.5

Figure 8: Variations of E_{str}/E_{Kirch} with w/w* for various h/R values: (a) 0.1, (b) 0.3, and (c) 0.5.

of Eq. 14 was correct. However, the formula curve deviated from our numerical simulation data in some regions. When $h/R \leq 0.2$, the simulation data appeared above the formula curve. When $0.2 < h/R \leq 0.35$, the simulation data and formula curve almost coincided. When $0.35 < h/R \leq 0.5$, the simulation data appeared above the formula curve. To explain this phenomenon, we re-emphasize the ratio of Kirchhoff strain energy to the in-plane stretch elasticity and consider a value of h/R in the above three cases, taking the ratio of the actual width to the critical width w/w* as the independent variable and the ratio of two kinds of energy E_{str}/E_{kirch} as the dependent variable, which are plotted in Fig. 8.

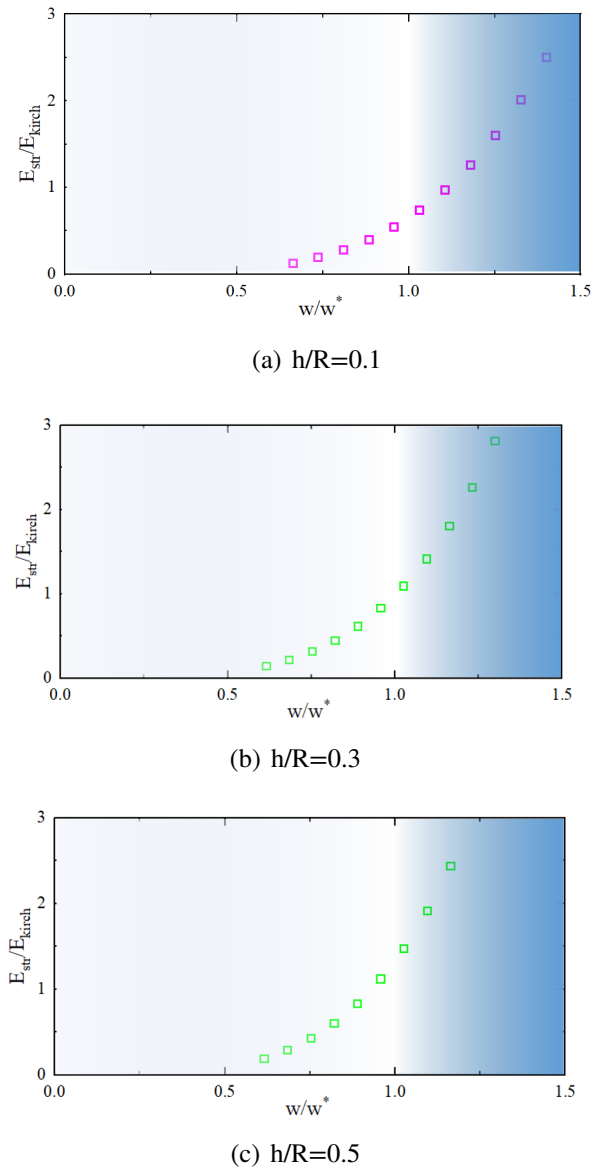The ratio of the in-plane stretch elasticity E_{str} and Kirchhoff strain energy E_{kirch} was not always the value predicted by Sano as 1, as it was affected by the length-to-thickness ratio of rgw ribbon. The data showed that the value of E_{str}/E_{kirch} at the "flipping point" gradually increased with the increase in the dimensionless quantity h/R. When the actual width of ribbon was close to the critical width for the corresponding thickness, the ratio of the in-plane stretching elasticity E_{str} and Kirchhoff strain energy E_{kirch} was not always the value predicted by Sano, as it was affected by the width-to-thickness

ratio of ribbon. The data show that the value of E_{str}/E_{kirch} at the "flipping point" gradually increased with the increase in the dimensionless quantity h/R.

4.2. Dimensional analysis and fitting of critical width w^* of rectangular section

To determine the critical width of the rectangular section, we focus on Eq. 14 again and use dimensional analysis (Sun,2016). Two dimensionless quantities are considered first:

$$\Pi_1 = \frac{h}{R}, \Pi_2 = \frac{w^*}{R}.$$

According to Buckingham's dimensional analysis theory, we can determine that $\Pi_2 = f(\Pi_1)$, which can be written as follows:

$$\frac{w^*}{R} = f(\frac{h}{R}).$$

Previous studies have shown that the functional relationship should be a power function, and the formula is rewritten as follows:

$$\frac{w^*}{R} = A \cdot (\frac{h}{R})^B.$$

where A and B are constants. Sano determined that $B = 0.5$. The finite element simulation data presented above were fitted to determine the value of A, as shown in Fig. 9. When B was fixed at 0.5, the fitting formula was as follows:

$$\frac{w^*}{R} = 2.22 \left(\frac{h}{R}\right)^{0.5}.$$

The coefficient of determination $R^2 = 0.98374$, the sum of squares of the residual was 0.00371, and the value of A was 2.22, which was very close to the prediction result of Sano. However, this result was still not sufficiently accurate. Our previous study showed that the influence of the ratio of the length to thickness on the critical width should not be 0.5. Thus, we eliminated the constraint on B and fit the data again with two free parameters, as shown in Fig. 10. The new fitting formula was as follows:

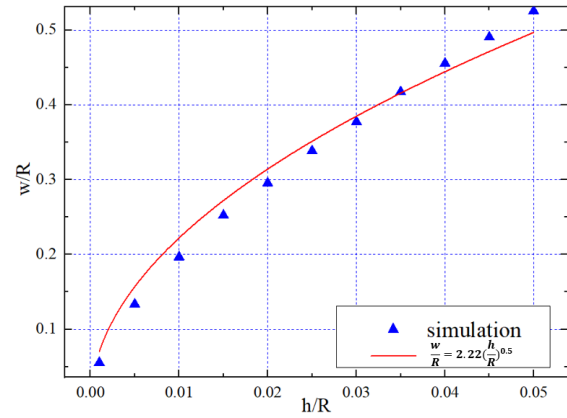$$\frac{w^*}{R} = 3.19 \left(\frac{h}{R}\right)^{0.6}.$$

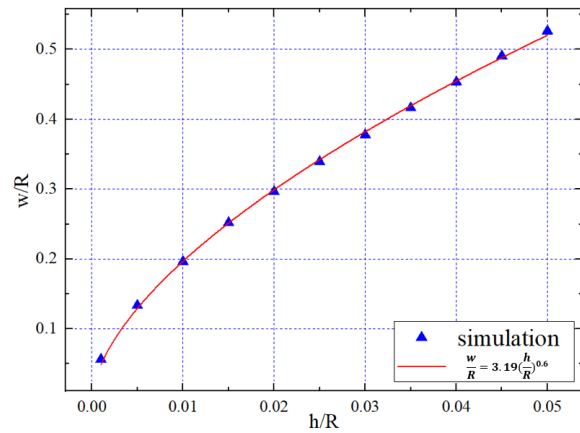**Figure 9:** Fitted curve to w^*/R when $B = 0.5$.

Figure 10: Fitted curve of w^*/R without parameter constraints.

The coefficient of determination was $R^2 = 0.99936$, and the sum of squared residuals was 1.46×10^{-4}. The value of A was 3.19, and the value of B was 0.6. This fit agreed more closely to the data than the first fit, which indicated that it was feasible to use dimensional analysis to solve this problem. In addition, we also carried out polynomial fitting. The coefficient of determination was $R^2 = 0.99631$, and the sum of squared residuals was 8.42×10^{-4}, which showed that the power function fit was more accurate than the polynomial fit.

4.3. Dimensional analysis and fitting of critical width w^* of elliptical cross section

We also explored the problem of the critical width of a ribbon with an elliptical cross section. We fit the finite element simulation data with the formula presented in the previous section, yielding

the following:
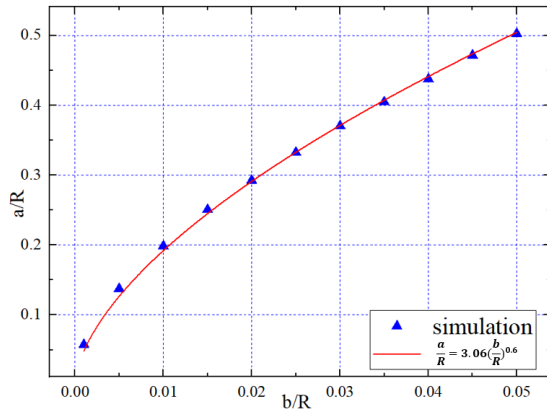
$$\frac{a^*}{R} = 3.06 \left(\frac{b}{R}\right)^{0.6}.$$

Figure 11: Fitted curve of w^*/R without parameter constraints.

In this case, $R^2 = 0.99830$, and the sum of squared residuals was 3.42×10^{-5}. Thus, the fitting was successful. Based on the results presented above, we found a general rule:

$$w^* = A \cdot R \left(\frac{h}{R}\right)^{0.6}.$$

For the critical widths of the ribbons with different cross sections, only the value of A changed, that is, the coefficient of the fitted equation. The coefficients A of the two cross sections are as follows:

	rectangle	ellipse
A	3.19	3.06

4.4. Efficiency of morphological transformation of ribbons with different cross sections

After studying the critical widths of the rectangular and elliptical cross sections, we focused on the efficiency of their morphological transformations during torsion. For comparison, we chose two cross sections in the simulation as follows: the length of the long axis of the ellipse was equal to the length of the rectangle, and the width of the short axis of the ellipse was equal to the width of the rectangle. The results are shown in the Fig. 12.

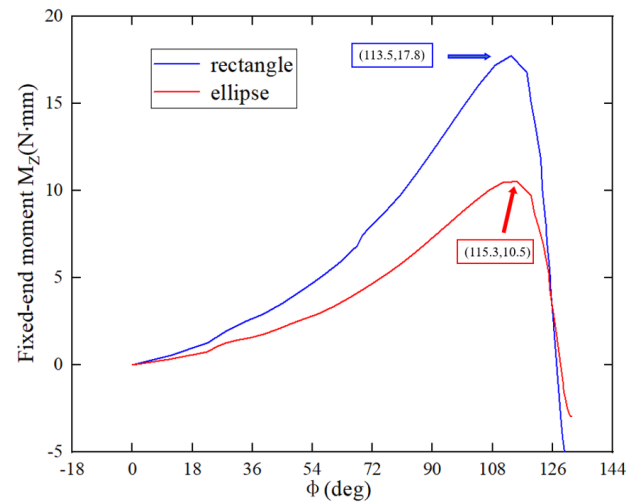The cross-sectional area of the ellipse was 21.5% less than that of the rectangle, while the fixed-end

Figure 12: Comparison of fixed-end bending moments of two kinds of cross sections.
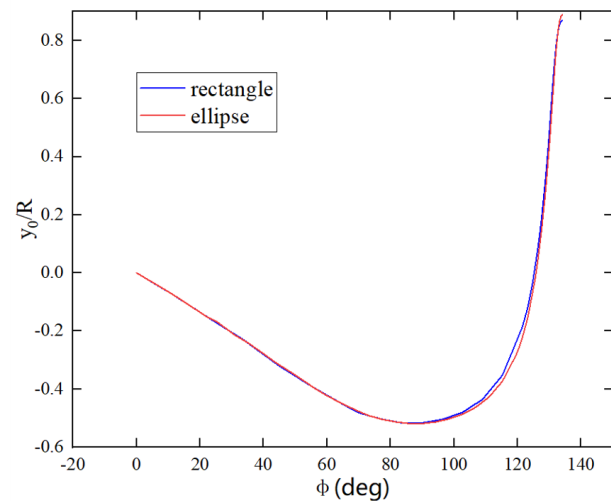

Figure 13: Comparison of deformation between two cross sections.

moment was 41% less. However, the deformation did not change significantly. This showed that when the ribbon of the elliptical cross section "flipped", the supports required less external force, and the same effect could be achieved. These results can be applied to many similar problems, indicating that the selection of the cross-section is very important for the morphological transformation of the ribbon structure.

5. Variation of out-of-plane deflection with support rotation angle during ribbon morphological transformation

Previously, we introduced Sano's research on the out-of-plane deflection, but the analysis only involved the deformation in the elastic energy storage stage of the arch ribbon, and a specific explanation of the out-of-plane deflection y_0 of the ribbon in the elastic energy release stage was not provided. Here, we consider 13 groups of ribbons with different widths, radii, and thicknesses through the control variable method. The specific sizes of the ribbons are shown in the table below. The effects of the radius, width, and thickness of the arched ribbon on y_0 during the ribbon morphological transformation were examined.

number	radius R(mm)	thickness h(mm)	width w(mm)
1	100	1	8
2	100	1	10
3	100	1	12
4	100	1	14
5	100	1	16
6	100	0.6	10
7	100	0.8	10
8	100	1.2	10
9	100	1.4	10
10	80	1	10
11	90	1	10
12	110	1	10
13	120	1	10

The numbers 1, 2, 3, 4, and 5 are group numbers, which were used to study the change of the displacement of the central point of the arched ribbon (s=0) in the y-direction with the rotation angle ϕ for various ribbon widths with the same radius and thickness, as shown in the Fig. 14. With the gradual increase in the width (still less than the critical width), the flipping point of the ribbon was advanced, the displacement changed more significantly, and the rate of change of the displacement relative to the rotation angle was also greater.

The numbers 2, 6, 7, 8, and 9 are group numbers that are used to study the change of the displacement of the center point of the arched ribbon along the y-direction with the change of the rota-
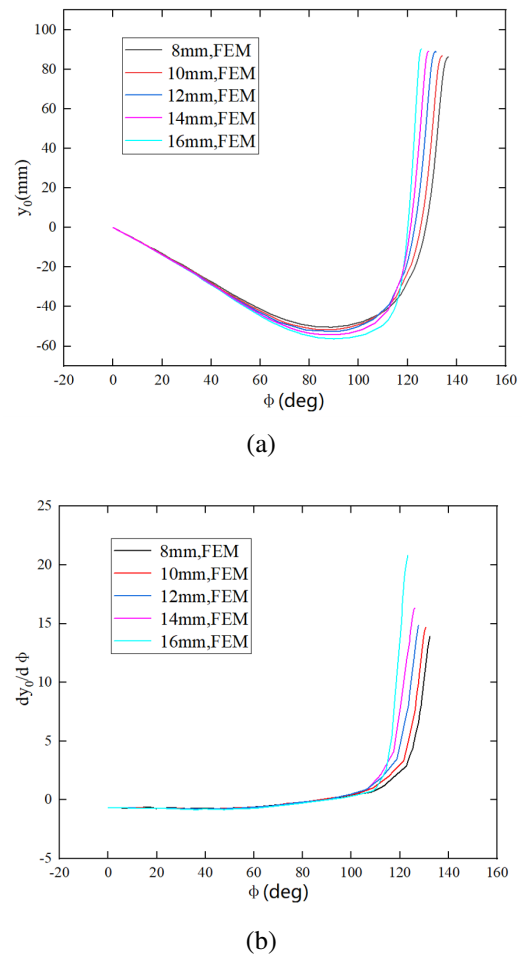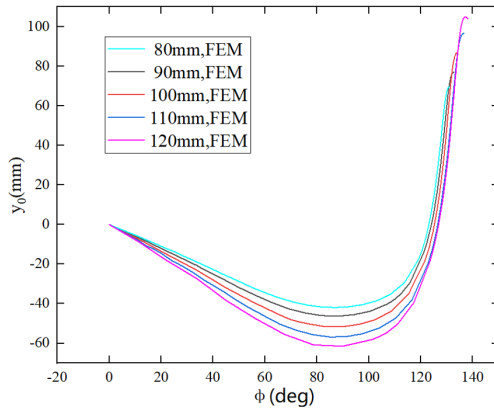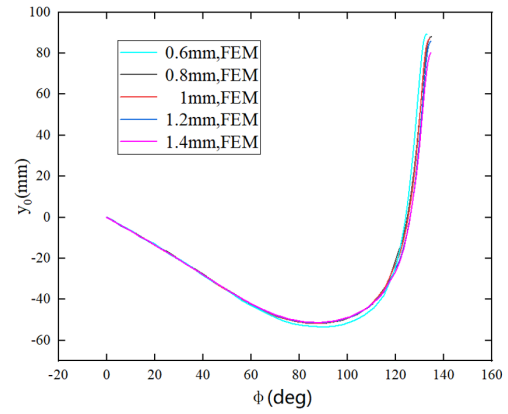

(a)

(b)

Figure 14: (a) Variation of the displacement y_0 with the rotation angle of the supports ϕ for various ribbon widths. (b) Variation of $dy_0/d\phi$ with the rotation angle of the supports ϕ for various ribbon widths.

tion angle ϕ for various radii of the ribbon with the same thickness and width, as shown in the figure below. As the radius of the arched ribbon gradually increased, the turning point of the arched ribbon did not change significantly, but the displacement changed greatly, indicating that an arched ribbon with a large radius could store more elastic deformation energy and convert it into kinetic energy.
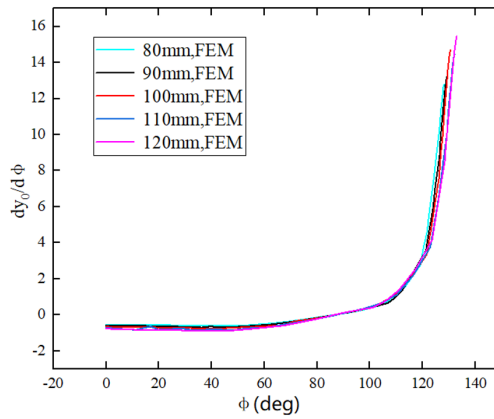
Groups 2, 4, 5, 12, and 13 were used to study the change of the displacement of the arched ribbon along the y-direction with the change of the flipping angle ϕ for various thicknesses of the arched ribbon with the same radius and width, as shown Fig. 16. There were no evident differences be-
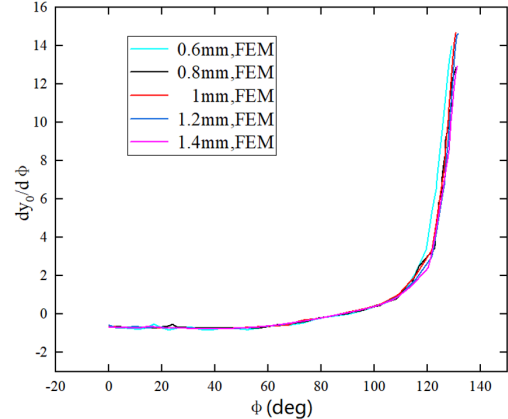
Figure 15: (a) Variation of the displacement y_0 with the rotation angle of the supports ϕ for various ribbon radii. (b) Variation of $dy_0/d\phi$ with the rotation angle of the supports ϕ for various ribbon radii.

Figure 16: (a) Variation of displacement y_0 with the rotation angle of the bearing ϕ for various ribbon thicknesses. (b) Variation of $dy_0/d\phi$ with the rotation angle of supports ϕ for various ribbon thicknesses.

tween the curves, indicating that the sensitivity of the structure to thickness was very low in the case of such a small thickness.

In summary, we concluded that for an arched ribbon driven by torsion, the radius and width of the ribbon are directly proportional to the rate of change of the displacement of the ribbon in the y-direction with the rotation angle of the support, and the increase in the radius and width in a certain range will cause the structure to store more elastic deformation energy, which can be converted into kinetic energy faster. At the same time, the increase in the width will advance the flipping time, while the thickness had little effect on the flipping time and displacement variation rate.

6. Conclusions

In this paper, based on the characteristics of an arched ribbon structure, a mathematical model of the arched ribbon dynamics driven by torsion was established using the Kirchhoff rod equation, which is shown in Eq. 6 and Eq. 7. Symmetry in Eq. 5 was also found, which could simplify the study of the dynamics of the ribbon. In this paper, the variations of the Euler angle of each point on the center line of the ribbon with s and ϕ are shown in Eq. 10, and the theoretical model was verified by the finite element method.

After verifying the theoretical model and Sano's experimental results with the finite element method, this paper further explored the changes of the crit-

ical width w^* when ribbons with different cross sections "flip" and "fold." Finally, a general formula for the critical width is presented: $w^* = A \cdot R \left(\frac{h}{R} \right)^{0.6}$. For rectangular sections, the coefficient A was 3.19; for elliptic cross sections, the coefficient A was 3.06.

When the morphological transformation of the ribbon with an elliptical cross section occurs, the work done by the external force is smaller than that of the ribbon with a rectangular cross section, and the same effect can be achieved. This can explain many similar problems, indicating that the selection of the cross section is very important for the morphological transformation of the ribbon structure.

For the arched ribbon driven by torsion, the radius R and width w of the ribbon are directly proportional to the change rate of the y-direction displacement of the ribbon relative to the support angle. At the same time, the increase of the width will advance the time at which the "flipping" occurs, while the thickness has little effect on the flipping time and displacement variation rate.

References

Armon, S., Aharoni, H., Moshe, M., Sharon, E., 2014. Shape selection in chiral ribbons: from seed pods to supramolecular assemblies. Soft Matter 10, 2733–2740.

Audoly, B., Neukirch, S., 2021. A one-dimensional model for elastic ribbons: a little stretching makes a big difference. hal-03132668 .

Chopin, J., Démery, V., Davidovitch, B., 1929. Roadmap to the morphological instabilities of a stretched twisted ribbon. In Jahresbericht der Deutschen Mathematiker- Vereinigung volume 39 (2. Abt. Heft 5/8), 49–51.

Deepak, T., Rahn, C.D., Kier, W.M., Walker, I.D., 2008. Soft robotics: Biological inspiration, state of the art, and future research. Applied Bionics and Biomechanics 5, 99–117.

Dill, E.H., 1992. Kirchhoff's theory of rods. Archive for History of Exact ences 44, 1–23.

Forterre, Y., 2013. Slow, fast and furious: Understanding the physics of plant movements. Journal of Experimental Botany 64, 4745–4760.

Fortorre, Y., Skotheim, J.M., Dumais, J., Mahadevan, L., 2005. How the venus flytrap snaps. Nature 433, 421–425.

Ghafouri, R., Bruinsma, R., 2005. Helicoid to spiral ribbon transition. Physical Review Letters 94, 138101.

Green, A.E., 1936. The equilibrium and elastic stability of a thin twisted strip. Royal Society of London Proceedings 154, 430–455.

Grossman, D., Sharon, E., Diamant, H., 2016. Elasticity and fluctuations of frustrated nano-ribbons. Physical Review Letters 116, 258105.

Holmes, D.P., Crosby, A., 2007. Snapping surfaces. Advanced Materials 19, 3589–3593.

Kirchhoff, G., 1859. Ueber das gleichgewicht und die bewegung eines unendlich dünnen elastischen stabes. Journal Für Die Reine Und Angewandte Mathematik 1859, 285–313.

Pomeau., Yves., 2010. Elasticity and Geometry. Oxford University Press.

Powers., Thomas, R., 2010. Dynamics of filaments and membranes in a viscous fluid. Reviews of Modern Physics 82, 1607–1607.

Sadowsky, M., 2016. Die differentialgleichungen des möbiusschen bandes. Journal of Elasticity 119.

Sano, T.G., Wada, H., 2019. Twist-induced snapping in a bent elastic ribbon. Physical Review Letters 122, 114301.1–114301.5.

Skotheim, J.M., Mahadevan, L., 2005. Physical limits and design principles for plant and fungal movements. Science 308, 1309–1310.

Sun, B., 2016. Dimensional Analysis and Lie Group. China High Education Press, Beijing (in Chinese).

Yu, T., Hanna, J.A., 2019. Bifurcations of buckled, clamped anisotropic rods and thin bands under lateral end translations. Journal of the Mechanics and Physics of Solids , S0022509617307469.

Yuk, H., Lin, S., Ma, C., Takaffoli, M., Fang, N.X., Zhao, X., 2017. Hydraulic hydrogel actuators and robots optically and sonically camouflaged in water. Nature Communications 8, 14230.